Journal of Materials Chemistry A

Depletion layer controls photocatalytic hydrogen evolution with p-type gallium phosphide particles

Journal:	*Journal of Materials Chemistry A*
Manuscript ID	TA-ART-06-2019-005879.R1
Article Type:	Paper
Date Submitted by the Author:	08-Jul-2019

Complete List of Authors:	Zhao, Zeqiong; University of California, Department of Chemistry Willard, Emma; UC Davis Dominguez, Julius; University of California, Department of Chemistry Wu, Zongkai; University of California, Department of Chemistry Osterloh, Frank ; University of California, Department of Chemistry

Depletion layer controls photocatalytic hydrogen evolution with p-type gallium phosphide particles

Zeqiong Zhao,[†] Emma J. Willard,[†] Julius R. Dominguez,[†] Zongkai Wu,[†] Frank E. Osterloh[,†]*

[†]Department of Chemistry, University of California Davis, One Shields Avenue, Davis, California 95616, United States

KEYWORDS: p-type semiconductor・photocatalyst・hydrogen evolution・depletion layer・surface photovoltage spectroscopy

ABSTRACT

P-type gallium phosphide (p-GaP) is an established photocathode material for hydrogen evolution, however, photocatalytic hydrogen evolution from p-GaP photocatalysts only proceeds with very low activity. The reason for the low activity of p-GaP, and of other p-type semiconducting photocatalysts, is presently unknown. To better understand this limitation, we have investigated the photocatalytic H_2 evolution activity and photovoltage generation of p-type GaP microparticles in the presence of sacrificial electron donors. Sub-micrometer sized particles with a Zn acceptor concentration of 5.5×10^{17} cm^{-3} were prepared by grinding a commercial p-type Zn:GaP wafer. According to surface photovoltage spectra, the p-GaP particles have an effective bandgap of 1.9 eV and generate a positive photovoltage of 0.41 V, due to movement of the holes in the space charge layer of the particles. After modification with a Ni_2P cocatalyst, p-GaP particles catalyze

H_2 evolution under visible light (> 400 nm, 400 mW·cm^{-2}) in the presence of various sacrificial electron donors. The highest hydrogen evolution rate of 13.5 μmol·h^{-1} was achieved with 0.05 M KI, followed by 3.6 μmol·h^{-1} with 0.05 M $K_4[Fe(CN)_6]$ and 0.5 μmol·h^{-1} with 0.05 M Na_2SO_3. Rates are inversely correlated with the standard reduction potential of the donors (more reducing donors give lower rates). This can be explained on the basis of depletion layer model at the p-GaP/electrolyte interface which prevents photoelectrons from reaching the Ni_2P cocatalyst. SPS measurements in the presence of the sacrificial reagents estimate the donor-dependent potential drop across the depletion layer as 0.25 - 0.45 V. This correlates well with logarithmic H_2 evolution rates, confirming that the depletion layer limits photochemical charge transfer. This model explains why p-type semiconductors have a much lower photocatalytic hydrogen evolution activity than n-type semiconductors. The SPS measurements also confirm electron trapping on the p-GaP surface as a reason for the slow deactivation of the photocatalysts.

Introduction

Overall water splitting with suspended photocatalysts is a promising option for large-scale hydrogen fuel production from sunlight.[1-6] Maximum light utilization is achieved in tandem or Z-scheme photocatalysts which connect light absorbing materials for the oxygen evolution reaction (OER) and hydrogen evolution reaction (HER) in series.[7-13] Ideally, the OER material should be a n-type semiconductor that can form a rectifying junction with the O_2/H_2O redox couple, and the HER material should be an p-type semiconductor that can form a junction with the H^+/H_2 redox couple.[1, 14] Interestingly, the number of known HER photocatalysts derived from p-type semiconductors is very small. Examples include Rh-doped $SrTiO_3$ [15] and La, Rh-codoped $SrTiO_3$ (AQY 30 % at 419 nm) [12, 13] and the $(CuGa)_{1-x}Zn_{2x}S_2$[16] solid solution (3% AQY at 420 nm) and $CuGaS_2$ (1.3 % at 380 nm).[17] The majority of p-type semiconductors, including p-GaP,[18] p-Cu_2O,[19]

p-WSe_2, [20] and p-Si [21] are active only as photoelectrodes but not as suspended particles.[22, 23] Understanding the reasons for the low activity and stability problems of suspended p-type photocatalysts is important because overcoming these limitations can enable a new generation of more efficient tandem photocatalysts for overall water splitting.

Among semiconductor photoelectrodes, p-GaP stands out due to its visible light active bandgap of 2.3 eV and its highly reducing conduction band edge at -1.0 V relative to the proton reduction potential.[24-27] Additionally, p-GaP photocathodes have been shown to reduce carbon dioxide,[28, 29] protons,[30] and split water into H_2 and O_2 without external bias when used in combination with a n-TiO_2 photoanode.[31] In contrast, suspended GaP particles [24] or nanowires [32] evolve H_2 at less than 0.2 $\mu mol \cdot h^{-1}$ after loading with the Pt cocatalyst. This falls short of the theoretical H_2 evolution limit of 0.19 $mmol \cdot h^{-1} \cdot cm^{-2}$ under standard solar illumination, assuming a band gap of 2.3 eV and quantum efficiency of 100%.

Here, we investigate the reasons for the low activity of p-GaP photocatalyst particles for the hydrogen evolution reaction, using p-GaP microparticles modified with dinickel phosphide (Ni_2P) as a model system.[33, 34] A commercial GaP wafer with known Zn-dopant concentration (5.5 x 10^{17} cm^{-3}) was used as a precursor to the particles. Photoelectrochemical measurements on the particle films and the wafer provide the photoonset and photocurrent for proton reduction, while surface photovoltage spectroscopy is used to measure the effective bandgap, majority charge carrier type, and the depletion layer potential drop. The combined measurements reveal that the hydrogen evolution rate and photovoltage of p-GaP particles are limited by a depletion layer, which directs minority carrier electrons to the GaP-liquid interface, toward the sacrificial donors and away from the hydrogen evolving cocatalyst. Meanwhile, the long-term stability of the photocatalyst is limited by electron trapping on the p-GaP surface.

Results and Discussion

P-type GaP particles with defined dopant concentrations are not yet accessible by lab scale synthesis. Therefore, such particles were obtained by grinding a commercial p-type Zn:GaP wafer with a 5.5×10^{17} cm^{-3} free hole charge carrier density. The p-GaP powder was characterized by powder X-ray diffraction (PXRD), scanning electron microscope (SEM), transmission electron microscope (TEM), and energy dispersive X-ray spectroscopy (EDX), as shown in **Figure 1** and **Figure S1**. The PXRD pattern of the p-GaP particles matches with the standard pattern of GaP cubic Zinc blende crystal structure (PDF #00-012-0191). From the SEM and TEM images, it can be seen that most particles have irregular shapes with sharp edges and corners, as expected for a product of grinding. The average particle size is 380 nm with a standard deviation of 340 nm. Based on the EDX results shown in **Figure S1**, the chemical composition of the p-GaP particles is $Ga_{0.515}P_{0.457}O_{0.027}$. The reduced phosphor content and enhanced oxygen content are the expected result of surface oxidation in air. UV-Vis diffuse reflectance spectra of the p-GaP wafer and of the particle powder are shown in **Figure 1f**. Linear extrapolation of the absorption onset gives an optical bandgap of 2.16 eV for the p-GaP particles and a band gap of 2.20 eV for the p-GaP wafer. These values agree well with the literature.[35, 36] The sub-bandgap absorption at 1.5 – 2.2 eV for the powder is attributed to transitions involving Zn states (0.07 eV above the GaP valence band) [37] and surface oxygen donor states (0.89 eV below the conduction band) [38] in p-GaP.[39] The latter absorption is increased due to the larger surface area of the powder.

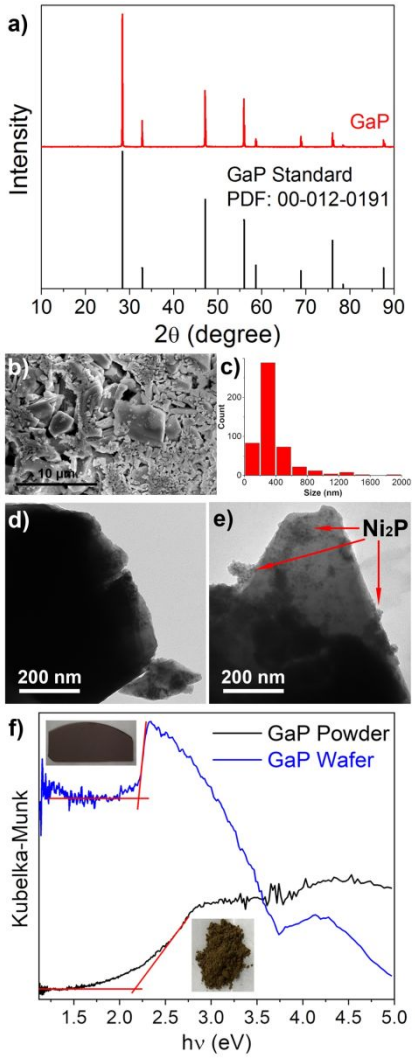

Figure 1 (a) Powder x-ray diffraction pattern, (b) SEM image, (c) size histogram, and (d) TEM image of obtained p-GaP particles. (e) TEM image of 4 wt% Ni_2P loaded p-GaP particles. (f) UV-Vis diffuse reflectance spectra and photos of p-GaP powder and p-GaP wafer. The shape of the wafer spectrum is an artefact of the diffuse reflection technique; it is caused by specular reflection of the incident light.

Photoelectrochemical scans for the p-GaP wafer immersed in air-free aqueous 0.1 M K_2SO_4 electrolyte are shown in **Figure 2a** and **Figure S2a**. The photocurrent reaches up to 7.5 $mA \cdot cm^{-2}$ at -1.07 V vs RHE, with a negligible dark current, and with an onset of 0.17 V vs RHE,

slightly positive of the proton reduction potential (0.00 V vs RHE). This onset is shifted cathodically with regard to the reported value (0.72 V vs RHE) for p-GaP wafers in 0.2 H_2SO_4 electrolyte.[30] The difference is attributed to the presence of an oxide layer on the p-GaP wafer. In contrast, the p-GaP particle film on FTO substrate in **Figure 2b** and **Figure S2b** has a much smaller photocurrent of ~20 μA·cm^{-2} at 0.0 V vs RHE, a significant dark current below 0.05 V vs RHE, and an anodically shifted onset potential of 0.42 V vs RHE. These are all consequences of the low packing density of the irregular p-GaP particles, which slows down charge transport through the film and which allows direct proton reduction at the FTO support. [40, 41]

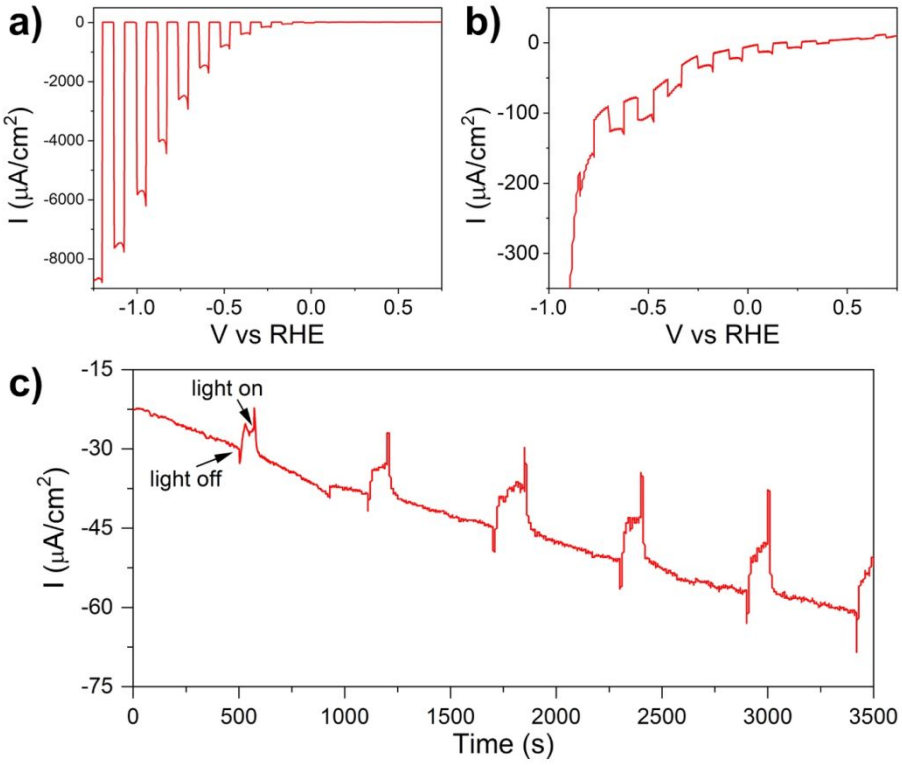

Figure 2 Photocurrent of (a) p-GaP wafer and (b) p-GaP particle film under chopped light (100 mW·cm^{-2}, unfiltered from Xe lamp) in degassed 0.1 M K_2SO_4 electrolyte. (c) Stability test of the photocurrent of p-GaP particle film at -0.08 V vs RHE.

Some of the observed current is due to cathodic corrosion of the enlarged p-GaP surface. This is confirmed with the photocurrent stability test shown in **Figure 2c.** Over the ~1h measurement period, the photocurrent of p-GaP remains relatively constant while the cathodic dark current increases continuously. This indicates that electrochemical reduction of the p-GaP particle film is taking place. According to Butler and Ginley, photocorrosion of GaP involves the formation of metallic Ga clusters, which can either leach into solution or accumulate on the GaP surface. [42, 43] In addition, there are strong capacitive currents in both the p-GaP particle film and the p-GaP wafer, as evident by the sawtooth shape of the photocurrent response after switching the light on.[44] The capacitive current is due to the trapping and de-trapping of photogenerated charge carriers at the p-GaP/electrolyte interface.[45]

Next, to study the photophysics of the p-GaP in the absence of an electrolyte, surface photovoltage spectroscopy (SPS) measurements were conducted on the p-GaP wafer and on a p-GaP particle film on FTO substrate in vacuum. The SPS spectrum for the p-GaP wafer (**Figure 3a** and **Figure S3**) shows a positive photovoltage with an onset of 2.0 eV and a maximum photovoltage of 0.41 V at 3.6 eV. The photo-onset at 2.0 eV is red-shifted compared to the reported value of 2.19 eV for an n-type GaP wafer.[46] We attribute the shift to excitation of Zn and surface O states in p-GaP, as mentioned above. In general, the surface photovoltage of flat semiconductor wafers can be attributed to light induced carrier separation in the depletion region of the wafer, as shown in the inset in **Figure 3a**.[47-49] A depletion layer with a potential drop given by **Eq.1** forms near the surface when majority carriers of fermi energy E_F become trapped in surface states of energy E_T.

$$\phi_{sc} = E_F - E_T \quad (1)$$

Photogenerated charge carriers are separated by this electric field to produce a photovoltage that approximates the potential drop across the space charge layer (0.41 V in the case of **Figure 3a**).

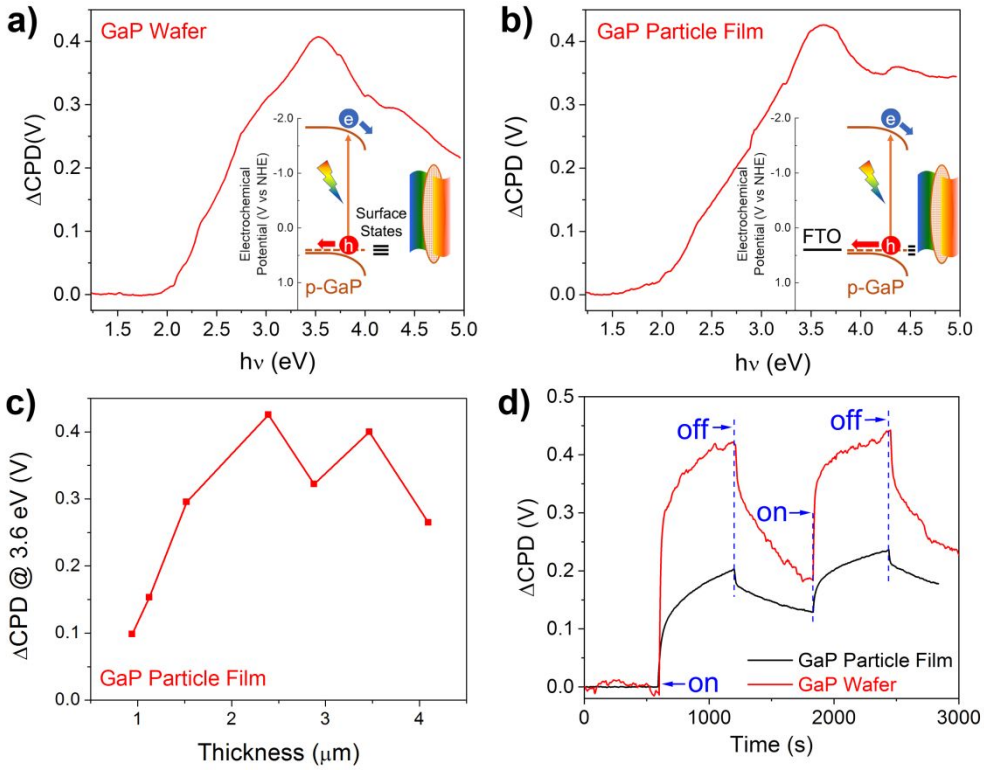

Figure 3 SPS spectra of (a) p-GaP wafer and (b) p-GaP particle film on FTO substrate with inserted energy diagram for the SPS process. Band edge positions are obtained from the literature.[35, 50] (c) Dependence of photovoltage under 3.6 eV illumination on p-GaP particle film thickness. (d) Time dependence of photovoltage under chopped irradiation at 3.4 eV with p-GaP wafer and p-GaP particle film.

In this way, the maximum photovoltage ΔCPD_{max} can be used to estimate the potential drop across the p-GaP depletion layer. Using $\Delta CPD_{max} = \phi_{sc} = 0.41$ V, the dielectric constant $\varepsilon = 11.1$, [37] and

the specified acceptor density of the wafer $N_A = 5.5 \times 10^{17}$ cm^{-3}, the space charge layer width *w* is 29 nm for the p-GaP wafer, according to **Eq. 2**. [51]

$$w = \sqrt{\frac{2\varepsilon_0\varepsilon_r}{eN_A}\left(\emptyset_{sc} - \frac{kT}{e}\right)} \quad (2)$$

According to the Gärtner model, photochemical charge separation is most effective when all photocarriers are generated within the space charge layer. [52-54] This is one reason why the maximum surface photovoltage in **Figure 3a** is observed at excitation energies near 3.6 eV. At this photon energy, the light penetration depth 1/α of the GaP wafer (20 nm based on the tabulated absorption coefficient of 4.99 x 10^5 cm at 3.6 eV) [36] matches the space charge layer. At lower photon energies, most of the light is absorbed deeper in the p-GaP wafer, where the electric field is zero and where carriers have to move by slower diffusion. Above 3.6 eV the photovoltage decreases due to the diminishing light intensity of the Xe lamp at higher photon energies.

The SPS spectrum for the p-GaP particle film in **Figure 3b** and **Figure S4** looks very similar to that of p-GaP wafer. The photovoltage onset at 1.9 eV is slightly lower, which indicates more sub-bandgap states in the p-GaP particles. These are a result of the increased surface area, as discussed above. This time the photovoltage is due to two components, one being the carrier separation in the space charge layer region of each individual particle, and the second one being majority carrier (hole) injection from the particle film into the FTO substrate (**Figure 3b** inset). Because the latter involves carrier transport through the entire film, the SPS data is film thickness dependent, as shown in **Figure 3c**. Photovoltage values at 3.6 eV first increase due to improved light absorption in the films and then slightly decrease due to less efficient charge transport through the film. This behavior has been previously observed for $BiVO_4$ and $CuBi_2O_4$ particle films.[49, 55] The maximum photovoltage of 0.42 V for the 2.4 μm thick particle film corresponds to optimal light absorption and carrier generation across the entire particle film. This agrees well with the

light penetration depth of GaP (2 μm at 2.75 eV using the tabulated absorption coefficient of 10^4 cm^{-1}). [36, 56] The photovoltage value at this thickness is 84% of the theory based on the energetics of the p-GaP/FTO system (**Figure 3b** inset). Based on the energy diagram, the majority of the photovoltage for the p-GaP particle film comes from the potential drop within the space charge layer of each particle.

The time dependence of the surface photovoltage under monochromatic illumination at 3.4 eV is shown in **Figure 3d**. Compared to particle films made of $BiVO_4$ [57] or $KCa_2Nb_3O_{10}$, [58] charge separation in the p-GaP wafer is relatively fast (25 seconds to reach 63% of final state). This indicates charge transport occurs not by *diffusion* but by *drift* in the electric field of the depletion layer. The photovoltage decay is markedly slower (44% of the photovoltage remain after 600 sec), which suggests that the electrochemical equilibrium to reform the original space charge layer occurs by carrier diffusion. For the p-GaP particle films, both photovoltage generation (~100 s) and decay (64% photovoltage remains after 600 s) are slower, due to the transport limitations through the film and because of the greater number of electron traps on the increased surface area of the particles. The large residual photovoltage suggests that cathodic photocorrosion due to electron trapping can occur even in the absence of an electrolyte.

To study the photocatalytic water reduction activity, 50 mg p-GaP particles were suspended in 50 mL 0.05 M aqueous potassium iodide solution at pH 7.2 and the mixture was irradiated with visible light. Iodide is a mild sacrificial electron donor with a defined standard reduction potential of +0.536 V vs NHE for the triiodide/iodiode redox couple.[59, 60] As shown in **Figure 4a**, the hydrogen evolution rate is only 1.4 $\mu mol \cdot h^{-1}$ under these conditions. This is attributed mainly to the slow proton reduction kinetics at the p-GaP surface which is known for its large proton reduction overpotential.[61] To overcome this problem, dinickel phosphide (Ni_2P)[33] was added as a

HER cocatalyst. Water-miscible Ni_2P nanoparticles were obtained via synthesis reported by Popczun *et al.* and capping agent exchange reported by Cao *et al*.[33, 62] As shown in **Figure S5**, the obtained Ni_2P nanocrystals show a matched PXRD pattern and an average diameter of ~10 nm, similar to the literature. The Ni_2P nanoparticles were loaded on p-GaP particles by physical mixing and ultrasonication in ethanol, followed by annealing at 450 °C under argon atmosphere. TEM images of p-GaP particles before and after loading of Ni_2P are shown in **Figure 1c** and **1d**. The particles are relatively evenly distributed on the p-GaP particles, which is also confirmed by EDS element maps shown in **Figure S6**. After addition of 1 wt% Ni_2P cocatalyst, photocatalytic H_2 evolution with p-GaP is enhanced to 5.7 $\mu mol \cdot h^{-1}$ (**Figure 4a**). Higher activity (13.5 $\mu mol \cdot h^{-1}$) is achieved with 4 wt% Ni_2P loaded p-GaP particles, but with 7 wt% Ni_2P the activity drops to 6.0 $\mu mol \cdot h^{-1}$, which is attributed to optical shielding from the Ni_2P cocatalyst. Also, H_2 evolution rates decrease over time, likely as a result of cathodic photocorrosion of p-GaP, as seen in the photoelectrochemical measurements and the SPS experiment. In order to raise the activity of the 4 wt% Ni_2P loaded p-GaP, $K_4[Fe(CN)_6]$ and Na_2SO_3 were tested as alternative sacrificial electron donors (**Figure 4b)** with slightly greater reducing power. [63, 64] However, these donors were found to be less active than KI (13.5 $\mu mol \cdot h^{-1}$), producing only 3.6 $\mu mol \cdot h^{-1}$ in the case of $K_4[Fe(CN)_6]$ and 0.5 $\mu mol \cdot h^{-1}$ with Na_2SO_3. This is counter-intuitive, considering that the reducing power of these reagents, and thus, the driving force for hole transfer to the sacrificial donor (see **Figure 4c**), increases in the order iodide (+0.536 V vs NHE) < hexacyanoferrate (II) (+0.358 V vs NHE) < sulfite (-0.51 V vs NHE at pH 7). The dependence of the H_2 evolution rates on the driving force for hole transfer is shown in **Figure 4d**. The plot is somewhat linear, as expected from the Butler Volmer equation for a thermodynamically controlled charge transfer process, however, the slope is negative, not positive. Such an inverse relationship between a proton reduction rate and its

driving force is reminiscent of the inverted Marcus regime for outer sphere electron transfer, where increasing driving force results in decreasing charge transfer rates.[51, 65-68] However, this theory cannot be applicable to the p-GaP particle proton reduction system for several reasons. First, the observed charge transfer processes occur under illumination involving simultaneous electron minority and hole majority transfer. Second, neither proton reduction at the photocatalyst nor iodide and sulfite oxidation are one electron outer sphere charge transfer processes.

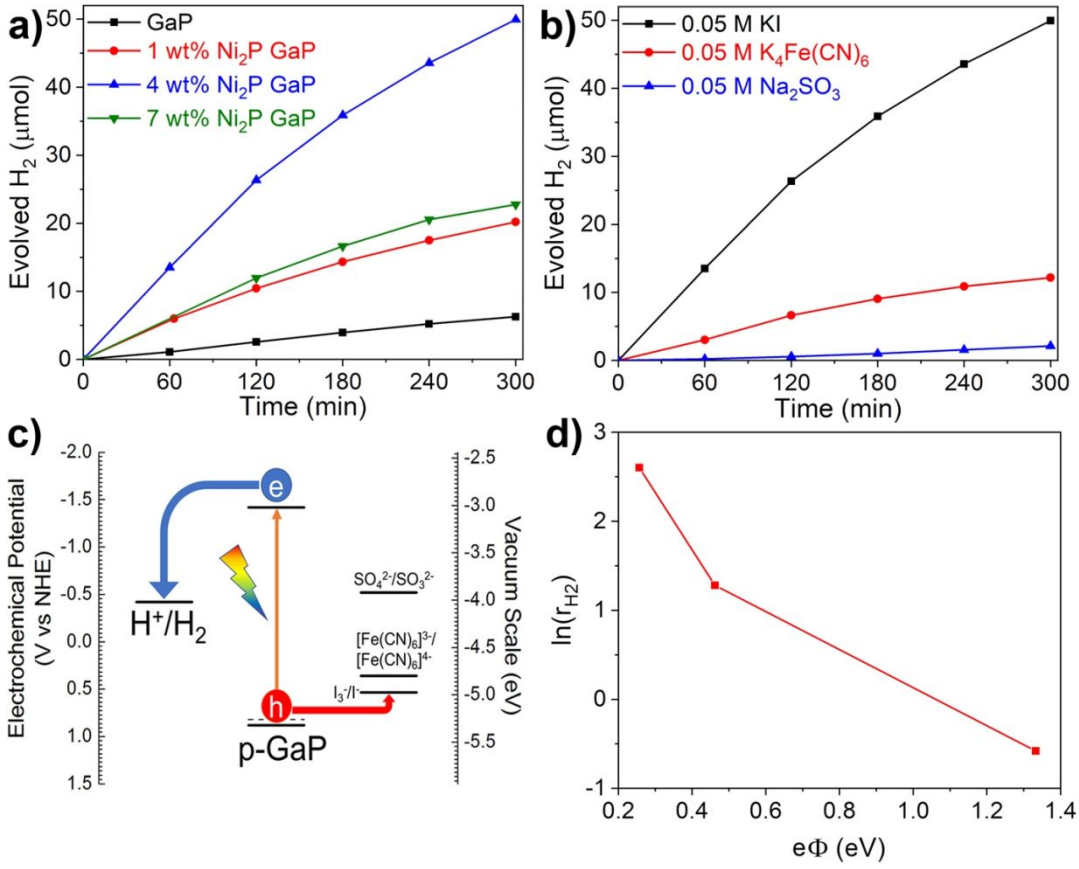

Figure 4 (a) Hydrogen evolution from 50 mg p-GaP particles with different Ni_2P loading amount in 50 mL solution under Xe lamp irradiation with 400 nm longpass filter in 0.05 M KI solution containing 0.05 M NaH_2PO_4 / 0.05 M Na_2HPO_4 at pH 7.2. (b) Hydrogen evolution from 50 mg of 4 wt% Ni_2P loaded p-GaP particles in 50 mL solution under Xe lamp irradiation with 400 nm

longpass filter. In all cases, a 0.05 M NaH_2PO_4 / 0.05 M Na_2HPO_4 buffer at pH 7.2 was used, with either 0.05 M KI, 0.05 M $K_4[Fe(CN)_6]$ or 0.05 M Na_2SO_3. (c) Energy diagram of p-GaP photocatalyzed water reduction process. (d) Plot of the logarithmic hydrogen evolution rate versus theoretical driving force for hole transfer according to (c).

Instead, the experimentally observed reactivity trend can be explained with the model in **Figure 5a**. When p-GaP particles are immersed in the reducing environment of the sacrificial electron donors, they become depleted of majority carrier holes and a depletion layer forms at the p-GaP/solution interface.

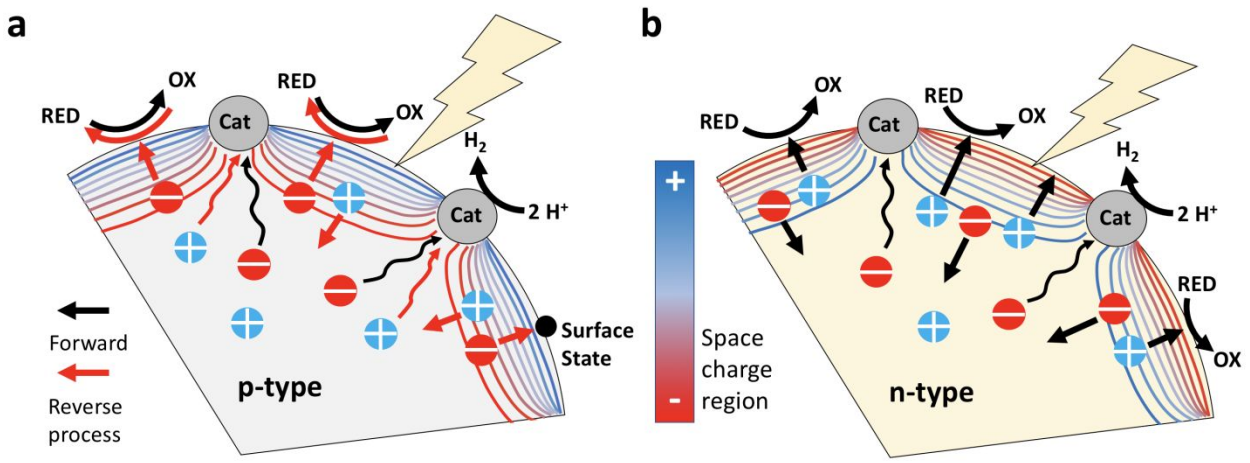

Figure 5 Depletion layer and charge carrier movement in illuminated a) p-type and b) n-type semiconductor/cocatalyst configurations in aqueous solutions of a reducing sacrificial agent. Potential lines are drawn after Garcia-Esparza et al.[69] Straight arrows indicate drift and wavy arrows indicate diffusion. Minority carriers (holes for n-type SC and electrons for p-type SC) generated inside the depletion layer are attracted to the surface, and away from the proton reduction cocatalyst (cat). For p-type semiconductors this promotes the back reaction (red arrows) and for n-type semiconductors the forward reaction (black arrows).

The polarity of that depletion layer is such that it sweeps electrons from the p-GaP interior to the p-GaP/liquid interface where they can react with GaP surface states or with the oxidized form of the sacrificial electron donor, e.g. triiodide is reduced to iodide or $[Fe(CN)_6]^{3-}$ is reduced to $[Fe(CN)_6]^{4-}$. These backward reactions are the reverse of the hydrogen evolving forward reaction. Electrons deep inside the p-GaP (away from the depletion layer) must reach the Ni_2P cocatalyst by diffusion. This process is slow because the electrons are minority carriers and their lifetime is short. Under these conditions, the forward reaction (proton reduction) will become less favorable as the potential drop in the depletion layer increases with more reducing electron donors. In the presence of a sacrificial electron donor, the potential drop ϕ_{sc} across the depletion layer is given by **Eq. 3**. Here, E^0 is the standard reduction potential of the sacrificial reagent and E_F is the p-GaP Fermi level.

$$\phi_{sc} = E_F/e\text{-}E^0 \quad (3)$$

More reducing reagents are expected to cause larger potential drops and wider depletion layers, promoting the backward reaction. In order to test this depletion layer hypothesis, the photovoltage of the p-GaP particle films was re-evaluated with SPS in the presence of the three sacrificial reagents. To minimize the effect of sample film variations, SPS experiments were performed on p-GaP particle films before and after addition of 0.05 mL 0.01 M sacrificial reagent solution, followed by drying in air. This coats the particle films with a layer of the sacrificial reagent, allowing observation of its photochemistry, as shown in previous work. [70, 71] As can be seen in **Figure 6**, addition of KI and of $K_4[Fe(CN)_6]$ diminishes the positive photovoltage of the p-GaP film, while addition of Na_2SO_3 increases it. The potential drop ϕ_{sc} at the p-GaP particles in contact with the sacrificial donors can be estimated from the photovoltage change in **Figure 6a** by adding the photovoltage change to the potential drop in the p-GaP wafer. This process eliminates the film

thickness dependence of the photovoltage signal. Measured photovoltage changes, calculated ϕ_{sc} values and corresponding space charge layer width are listed in **Table 1**.

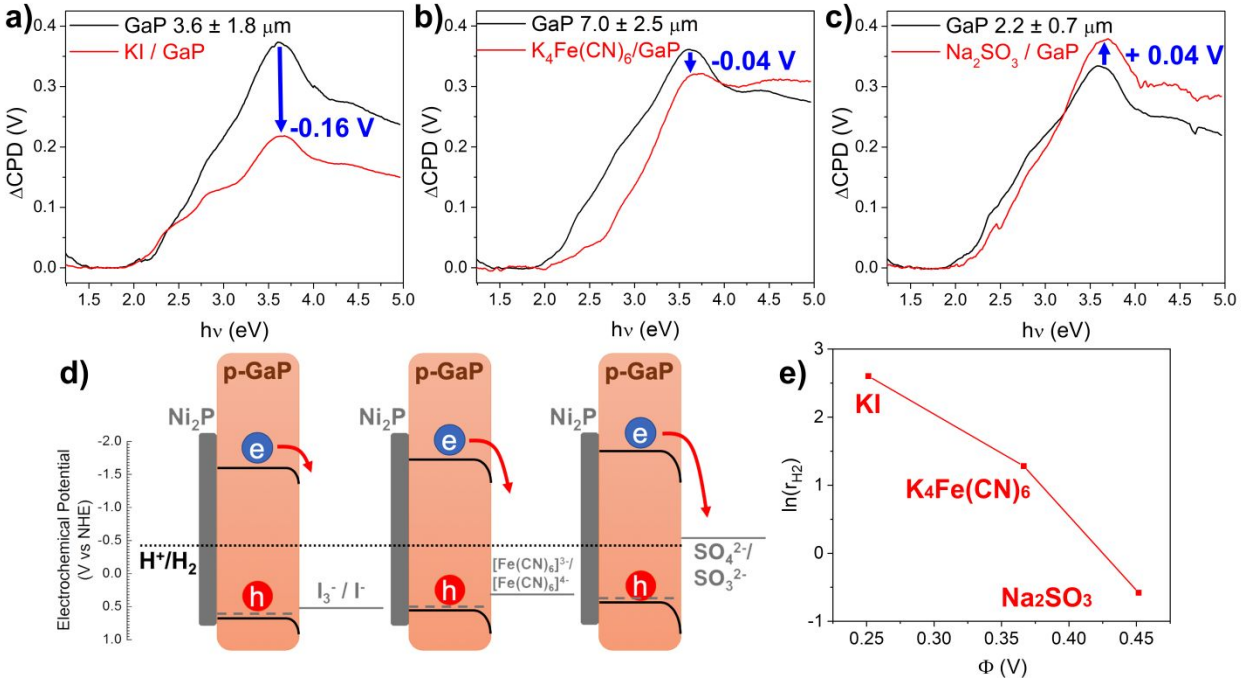

Figure 6 (a-c) SPS spectra of p-GaP particle films before and after sacrificial reagent treatment. P-GaP particle films were soaked in 0.01 M sacrificial reagent solution for 1 h, followed by addition of 0.05 mL of a 0.01 M solution on top and air drying. (d) Band bending and electron transfer at p-GaP/electrolyte interface. Ni_2P is assumed to form an Ohmic contact with p-GaP. (e) Plot of the logarithmic hydrogen evolution rate versus the potential drop across the depletion layer.

The data shows that KI and $K_4[Fe(CN)_6]$ decrease the depletion layer of the p-GaP particles, while addition of Na_2SO_3 increases it, compared to the non-coated p-GaP particles. This is also shown schematically in **Figure 6d**. Stronger reducing reagents not only increase the driving force for the back reaction but they also make the depletion layer wider, capturing more electrons from inside the p-GaP particles. An Arrhenius-like plot of the natural logarithm of the measured H_2 evolution

rate versus the calculated ϕ_{sc} values is shown in **Figure 6e**. The nearly linear correlation and the negative slope are expected for a reaction that is increasingly inhibited by the backward process. Deviations from linearity are most likely due to Fermi level pinning from the p-GaP surface states or from shading from the colored sacrificial reagents.

Table 1. Dimensions of the depletion layer in p-GaP particles

System	Photovoltage change / V *	Potential drop ϕ_{sc} / V *	Depletion layer width w/ nm from Eq.2
p-GaP /vacuum	-	0.41	29
p-GaP/ KI	-0.16	0.25	22
p-GaP / $K_4[Fe(CN)_6]$	-0.04	0.37	28
p-GaP / Na_2SO_3	0.04	0.45	31

* Calculated from: ϕ_{sc} = ΔCPD (p-GaP particle film treated with sacrificial reagent) - ΔCPD (p-GaP particle film) + ΔCPD (p-GaP wafer).

The model in **Figure 5** not only explains the low HER activity for p-type photocatalysts, but also the high activity of many n-type semiconductor photocatalysts [72] (such as ZnS, CdS, TiO_2, $SrTiO_3$, g-C_3N_4 [73]) for this reaction. For n-type semiconductors (**Figure 5b**), the space charge layer at the solid-liquid interface has the opposite polarity of a p-type SC. That means the electric field pulls hole minority carriers to the surface where they can react with the sacrificial donors. Also, the electrons n-semiconductors can reach the cocatalyst easily by diffusion because they are the *majority* carriers and have an extended lifetime. For p-type semiconductors, the polarity of the band bending and the shorter lifetime of the minority carriers inhibit the HER forward reaction.

Conclusions

In this work, we prepared p-GaP particles with average size of 380 ± 340 nm by grinding a commercial p-type Zn:GaP wafer. Photoelectrochemical measurement shows that the p-GaP wafer is stable from -2.0 to 2.0 V vs RHE in aqueous K_2SO_4 electrolyte while the p-GaP particle film shows cathodic dark current starting at 0.05 V vs RHE, due to reduction of surface states. SPS data on the particles confirm an effective bandgap of 1.9 eV, holes as the majority carrier, and surface trapping of electrons as a problem in p-GaP particles. Photocatalytic hydrogen evolution with Ni_2P modified p-GaP particles under visible light illumination proceeds with KI, $K_4[Fe(CN)_6]$, and Na_2SO_3 as sacrificial reagents, at low rates not exceeding 13.5 $\mu mol \cdot h^{-1}$ and with significant decline due to cathodic photocorrosion. The observed inverse dependence of HER rates on the reducing power of the electron donors can be explained on the basis of the depletion layer at the p-GaP/liquid interface, which pulls electrons away from the HER cocatalyst and into p-GaP surface states. According to surface photovoltage measurements, the depletion layer is 22-31 nm thick and has a donor-dependent barrier height of 0.25 eV (KI), 0.37 eV (K_4FeCN_6), and 0.45 eV (Na_2SO_3). The depletion layer model not only explains the low activity of p-type semiconducting photocatalysts but also the higher activity of n-type semiconducting photocatalysts. We expect these findings to aid the development of p-type and tandem photocatalysts for solar energy driven hydrogen generation from water.

EXPERIMENTAL

P-type zinc doped gallium phosphide wafer (0.164 ohm·cm, EL-CAT Inc., carrier density 5.5 x 10^{17} cm^{-3}), nickel (II) 2,4-pentanedionate (95%, Alfa-Aesar), tri-octylphosphine (90%, Aldrich), oleylamine (approximate C18-content 80-90%, 97% (primary amine-value), Acros

Organics), 1-octadecene (90%, Aldrich), hexane (Sigma-Aldrich, for HPLC, > 98.5%), chloroform (Fisher, HPLC grade), methanol (Sigma-Aldrich, ACS reagent, >99.8%), acetone (Sigma-Aldrich, for HPLC, >99.9%), polyvinylpyrrolidone (Aldrich, M_w 55,000), sodium sulfite (Sigma-Aldrich, ACS reagent, >98.0%), potassium iodide (99.9%, Fisher Scientific), potassium hexacyanoferrate (II) trihydrate (99%, Sigma-Aldrich), sodium phosphate monobasic monohydrate (Sigma-Aldrich, 98.0% - 102.0%), sodium phosphate dibasic heptahydrate (Sigma-Aldrich, 98% - 102.0%), compress nitrogen and argon gas (99.999%, Praxair) were used as received. Water was purified to 18 MΩ·cm resistivity by a Nanopure system.

P-type gallium phosphide particles were prepared by manually grinding 1.0 g of a commercial p-type Zn:GaP wafer with an agate mortar and pestle for 1 hours in air. The obtained powder was stored in a closed container in air.

Dinickel phosphide (Ni_2P) nanoparticles were synthesized via an air-free reaction.[33] 250 mg $Ni(acac)_2$ (0.98 mmol), 4.5 mL 1-octadecene (14.1 mmol), 6.4 mL oleylamine (19.5 mmol) and 2 mL tri-octylphosphine (4.4 mmol) was added to a 50 mL three-necked, round bottom flask containing a stir bar. The flask was equipped with a thermometer adapter, thermocouple, Liebig condenser, and an adaptor connected to a nitrogen tank. N_2 gas was flushed into the flask for 30 min before heating. The reaction mixture was then stirred moderately and was heated for 1 h at 120 °C under N_2 to remove water and other low-boiling impurities using a heating mantle. Afterwards, the solution was heated to 320 °C for 2 h. The reaction was then cooled slowly by turning off the heating mantle until the solution reached 200 °C, after which the flask was removed from the heating mantle to achieve rapid cooling to room temperature. The reaction mixture was transferred into centrifuge tubes, followed by centrifugation at 7000 rpm for 5 min. The isolated powder was re-suspended using 1:3 (v:v) hexanes:ethanol and then centrifuged again. This process

was repeated for three times after which the powder was re-suspended using pure hexanes and centrifuged one final time. The resulting black Ni_2P powder was vacuum dried and stored in a nitrogen filled glovebox.

Water-soluble Ni_2P nanoparticles capped with poly(vinylpyrrolidone) (PVP) were obtained by ligand exchange.[62] 5 mg Ni_2P nanoparticles were dissolved in 1 mL hexanes. 25 mL chloroform containing 0.1 g PVP was added to the hexanes solution and then heated to 60 °C for 5 h under N_2 atmosphere. Acetone was added to the mixture after it was cooled to room temperature. The black powder was isolated by centrifugation and then washed with acetone three times. The PXRD pattern of Ni_2P nanoparticles matches well with the standard pattern of Ni_2P (ICDD PDF #00-074-1385), as shown in **Figure S4**.

Ni_2P loaded p-GaP was prepared by the following procedure. 4 mg Ni_2P nanoparticles and 100 mg p-GaP particles were suspended in 10 mL ethanol. The mixture was sonicated for 4 h and then ground with a pestle and mortar for 30 min under air. After all ethanol was vaporized, the resulting solid was annealed in a tube furnace at 450 °C for 3 h under Ar gas atmosphere with a flow rate of 28 mL· min^{-1}.

Transmission electron microscopy (TEM) images were recorded using a FEI L120C TEM at 80 kV. Sample suspensions were dropped onto carbon coated Cu-grids and allowed to dry in air naturally. Scanning electron microscopy (SEM) and energy dispersive X-ray spectroscopy (EDX) were recorded using Schios DualBeam SEM/FIB. Sample suspensions were dropped onto silicon wafer and allowed to dry in air naturally. Powder X-ray diffraction measurements were performed using a Bruker D8 Advance Eco with a Cu Kλ X-ray radiation and a monochromatic wavelength of 1.5418 Å. UV-Vis diffuse reflectance spectra were recorded on a Thermo Scientific Evolution 220 UV Vis spectrometer equipped with an integrating sphere.

For photoelectrochemical measurements, a p-GaP wafer or p-GaP particle film working electrode was used in a three electrode cell together with a Pt counter electrode and a saturated calomel reference electrode (SCE). Aqueous electrolyte solution (0.1 M K_2SO_4) were added to the cell and degassed with N_2 gas for 15 min to remove all dissolved oxygen prior to scanning. The system was calibrated versus RHE using the redox potential of $K_4[Fe(CN)_6]$ at +0.358 V vs. RHE. A Xe lamp was used as the light source with a 400 nm long pass filter with a light intensity of 100 $mW \cdot cm^{-2}$ at the flask surface.

Surface photovoltage spectroscopy (SPS) measurements were conducted under vacuum (2.5×10^{-4} mBar) on a p-GaP wafer and p-GaP particle films on FTO substrate. A gold Kelvin probe (Delta PHI Besocke) served as the reference electrode. Samples were illuminated with monochromatic light from a 150 W Xe lamp filtered through an Oriel Cornerstone 130 monochromator (1-10 $mW \cdot cm^{-2}$). The measured contact potential difference (CPD) values were corrected for drift effects by subtracting a dark scan and to yield the ΔCPD values plotted in **Figures 3** and **5**. To prepare the p-GaP film samples, fluorine-doped tin oxide (FTO) substrates were sonicated sequentially in acetone, methanol and 2-propanol, rinsed with water, and dried in air before use. In general, 10 mg of the particles were suspended in 1 mL ethanol and then sonicated for 3 h. Then 0.02 mL of this suspension was dropped on FTO substrate with a scotch tape circle mask with diameter of 7 mm. More suspensions were added if thicker films were desired. The films were then heated at 450 °C for 3 h under Ar with a flow rate of 28 $mL \cdot min^{-1}$ before measurement. For sacrificial reagent experiments, the films were first soaked in the respective 0.01 M solutions for 1 h, followed by addition of 0.05 mL of a 0.01 M solution on top and drying in air overnight. Film thicknesses were measured using a Dektak 150 profilometer after the SPS measurement.

Photocatalytic hydrogen evolution tests were performed by dispersing 50 mg of the catalysts in aqueous solutions of the sacrificial reagents in a 135 mL quartz glass flask. Reaction mixtures were degassed with N_2 for 15 min to remove the residual oxygen dissolved in the water. The flask was purged with argon and irradiated with a 300 W xenon arc lamp attached with a sodium nitrite 400 nm long pass filter (400 $mW \cdot cm^{-2}$ at the flask surface as measured by an International Light IL1400BL photometer equipped with a GaAsP detector for 280 to 660 nm sensitivity range). The airtight irradiation system was connected to a calibrated Varian 3800 gas chromatograph (with a 60/80 Å molecular sieve column and thermal conductivity detector) to identify and quantify the evolved gases.

CONFLICTS OF INTEREST

There are no conflicts to declare.

ACKNOWLEDGMENT

This work was supported by the U. S. Department of Energy, Office of Science, Office of Basic Energy Sciences under Award Number DE- SC0015329.

SUPPLEMENTAL INFORMATION

Electronic supplementary information (ESI) available: Elemental analysis data, surface photovoltage spectra, electrochemical data, X-ray diffraction patterns, SEM images, and H_2/O_2 evolution results.

REFERENCES

1. F. E. Osterloh, in *Integrated Solar Fuel Generators*, The Royal Society of Chemistry, 2019, DOI: 10.1039/9781788010313-00214, pp. 214-280.
2. D. M. Fabian, S. Hu, N. Singh, F. A. Houle, T. Hisatomi, K. Domen, F. E. Osterloh and S. Ardo, *Energ. & Envi. Sci.*, 2015, **8**, 2825-2850.
3. B. D. James, G. N. Baum, J. Perez and K. N. Baum, http://www1.eere.energy.gov/hydrogenandfuelcells/pdfs/pec_technoeconomic_analysis.pdf).
4. S. Haussener, C. Xiang, J. M. Spurgeon, S. Ardo, N. S. Lewis and A. Z. Weber, *Energ. & Environ. Sci.*, 2012, **5**, 9922-9935.
5. J. W. Ager, M. R. Shaner, K. A. Walczak, I. D. Sharp and S. Ardo, *Energ. & Environ. Sci.*, 2015, **8**, 2811-2824.
6. A. C. Nielander, M. R. Shaner, K. M. Papadantonakis, S. A. Francis and N. S. Lewis, *Energ. & Environ. Sci.*, 2015, **8**, 16-25.
7. A. Kudo, *MRS Bulletin*, 2011, **36**, 32-38.
8. K. Maeda, *ACS Catalysis*, 2013, **3**, 1486-1503.
9. T. Hisatomi, J. Kubota and K. Domen, *Chem. Soc. Rev.*, 2014, **43**, 7520-7535.
10. M. A. Melo, Z. Wu, B. A. Nail, A. T. De Denko, A. F. Nogueira and F. E. Osterloh, *Nano Lett.*, 2018, **18**, 805-810.
11. H. Kato, Y. Sasaki, N. Shirakura and A. Kudo, *J. Mater. Chem. A*, 2013, **1**, 12327-12333.
12. Q. Wang, T. Hisatomi, Y. Suzuki, Z. Pan, J. Seo, M. Katayama, T. Minegishi, H. Nishiyama, T. Takata, K. Seki, A. Kudo, T. Yamada and K. Domen, *J. Am. Chem. Soc.*, 2017, **139**, 1675-1683.
13. Q. Wang, T. Hisatomi, Q. Jia, H. Tokudome, M. Zhong, C. Wang, Z. Pan, T. Takata, M. Nakabayashi, N. Shibata, Y. Li, I. D. Sharp, A. Kudo, T. Yamada and K. Domen, *Nat. Mater.*, 2016, **15**, 611–615.
14. A. J. Nozik, *Appl. Phys. Lett.*, 1977, **30**, 567-569.
15. K. Iwashina and A. Kudo, *J. Am. Chem. Soc.*, 2011, **133**, 13272-13275.
16. T. Kato, Y. Hakari, S. Ikeda, Q. Jia, A. Iwase and A. Kudo, *J. Phys. Chem. Lett.*, 2015, **6**, 1042-1047.
17. K. Iwashina, A. Iwase, Y. H. Ng, R. Amal and A. Kudo, *J. Am. Chem. Soc.*, 2015, **137**, 604-607.
18. S. Hu, M. R. Shaner, J. A. Beardslee, M. Lichterman, B. S. Brunschwig and N. S. Lewis, *Science*, 2014, **344**, 1005-1009.
19. P. E. de Jongh, D. Vanmaekelbergh and J. J. Kelly, *Chem. Commun.*, 1999, 1069-1070.

20. J. M. Velazquez, J. John, D. V. Esposito, A. Pieterick, R. Pala, G. Sun, X. Zhou, Z. Huang, S. Ardo, M. P. Soriaga, B. S. Brunschwig and N. S. Lewis, *Energ. & Environ. Sci.*, 2016, **9**, 164-175.
21. S. W. Boettcher, E. L. Warren, M. C. Putnam, E. A. Santori, D. Turner-Evans, M. D. Kelzenberg, M. G. Walter, J. R. McKone, B. S. Brunschwig, H. A. Atwater and N. S. Lewis, *J. Am. Chem. Soc.*, 2011, **133**, 1216-1219.
22. A. Kudo and Y. Miseki, *Chem Soc Rev*, 2009, **38**, 253-278.
23. Z. S. Li, W. J. Luo, M. L. Zhang, J. Y. Feng and Z. G. Zou, *Energ Environ Sci*, 2013, **6**, 347-370.
24. J. Sun, C. Liu and P. Yang, *Journal of the American Chemical Society*, 2011, **133**, 19306-19309.
25. A. B. Ellis, J. M. Bolts, S. W. Kaiser and M. S. Wrighton, *J. Am. Chem. Soc.*, 1977, **99**, 2848-2854.
26. A. Bourrasse and G. Horowitz, *Journal De Physique Lettres*, 1977, **38**, L291-L293.
27. S. Hlynchuk, M. M. MacInnes and S. Maldonado, *J. Phys. Chem. C*, 2018, **122**, 20073-20082.
28. M. Halmann, *Nature*, 1978, **275**, 115-116.
29. E. E. Barton, D. M. Rampulla and A. B. Bocarsly, *J. Am. Chem. Soc.*, 2008, **130**, 6342-+.
30. A. J. Nozik, *Appl. Phys. Lett.*, 1976, **29**, 150-153.
31. A. J. Nozik, *Appl. Phys. Lett.*, 1976, **29**, 150-153.
32. J. W. Sun, C. Liu and P. D. Yang, *J. Am. Chem. Soc.*, 2011, **133**, 19306-19309.
33. E. J. Popczun, J. R. McKone, C. G. Read, A. J. Biacchi, A. M. Wiltrout, N. S. Lewis and R. E. Schaak, *Journal of the American Chemical Society*, 2013, **135**, 9267-9270.
34. T. F. Jaramillo, K. P. Jørgensen, J. Bonde, J. H. Nielsen, S. Horch and I. Chorkendorff, *Science*, 2007, **317**, 100-102.
35. A. Standing, S. Assali, L. Gao, M. A. Verheijen, D. van Dam, Y. Cui, P. H. L. Notten, J. E. M. Haverkort and E. P. A. M. Bakkers, 2015, **6**, 7824.
36. D. E. Aspnes and A. A. Studna, *Phys. Rev. B*, 1983, **27**, 985-1009.
37. O. Madelung, *Semiconductors: Data Handbook*, Springer, Berlin, 3rd edn., 2004.
38. P. J. Dean and C. H. Henry, *Physical Review*, 1968, **176**, 928-937.
39. S. D. Lacey, *Sol. State Comm.*, 1970, **8**, 1115-1118.
40. G. Hodes, I. D. J. Howell and L. M. Peter, *J. Electrochem. Soc.*, 1992, **139**, 3136-3140.
41. O. C. Compton and F. E. Osterloh, *J. Phys. Chem. C*, 2009, **113**, 479-485.
42. M. A. Butler and D. S. Ginley, *J. Electrochem. Soc.*, 1980, **127**, 1273-1278.
43. E. S. Brown, S. L. Peczonczyk, Z. Wang and S. Maldonado, *J. Phys. Chem. C*, 2014, **118**, 11593-11600.
44. J. Wang and F. E. Osterloh, *Journal of Materials Chemistry A*, 2014, **2**, 9405-9411.
45. J. Wang and F. E. Osterloh, *J. Mater. Chem. A*, 2014, **2**, 9405-9411.

46. B. Adamowicz and J. Szuber, *Surf. Sci.*, 1991, **247**, 94-99.
47. L. Kronik and Y. Shapira, *Surface Science Reports*, 1999, **37**, 1-206.
48. J. Lagowski, *Surface Science*, 1994, **299-300**, 92-101.
49. Y. Yang, J. Wang, J. Zhao, B. A. Nail, X. Yuan, Y. Guo and F. E. Osterloh, *ACS Applied Materials & Interfaces*, 2015, **7**, 5959-5964.
50. A. Krawicz, D. Cedeno and G. F. Moore, *Physical Chemistry Chemical Physics*, 2014, **16**, 15818-15824.
51. R. Krol, *Photoelectrochemical Hydrogen Production*, 2012, **102**, 13-67.
52. W. W. Gärtner, *Physical Review*, 1959, **116**, 84-87.
53. S. Soedergren, A. Hagfeldt, J. Olsson and S.-E. Lindquist, *J. Phys. Chem. C.*, 1994, **98**, 5552-5556.
54. L. M. Peter, in *Photocatalysis: Fundamentals and Perspectives*, The Royal Society of Chemistry, 2016, DOI: 10.1039/9781782622338-00001, pp. 1-28.
55. G. Sharma, Z. Zhao, P. Sarker, B. A. Nail, J. Wang, M. N. Huda and F. E. Osterloh, *Journal of Materials Chemistry A*, 2016, **4**, 2936-2942.
56. W. G. Spitzer, M. Gershenzon, C. J. Frosch and D. F. Gibbs, *J. Phys. Chem. Solids*, 1959, **11**, 339-341.
57. Y. Yang, J. Wang, J. Zhao, B. A. Nail, X. Yuan, Y. Guo and F. E. Osterloh, *ACS Appl. Mater. & Interfaces*, 2015, **10**, 5959–5964.
58. J. Zhao and F. E. Osterloh, *J. Phys. Chem. Lett*, 2014, **5**, 782–786.
59. Y. I. Kim, S. Salim, M. J. Huq and T. E. Mallouk, *J. Am. Chem. Soc.*, 1991, **113**, 9561-9563.
60. P. Vanysek, in *CRC Handbook of Chemistry and Physics*, CRC Press/Taylor and Francis, Boca Raton, FL, 88 (Internet Version 2008) edn., 2008.
61. B. C. Wood, E. Schwegler, W. I. Choi and T. Ogitsu, *Journal of the American Chemical Society*, 2013, **135**, 15774-15783.
62. S. Cao, Y. Chen, C. J. Wang, P. He and W. F. Fu, *Chem Commun*, 2014, **50**, 10427-10429.
63. S. N. Frank and A. J. Bard, *J. Am. Chem. Soc.*, 1977, **99**, 4667-4675.
64. J. F. Reber and K. Meier, *J. Phys. Chem.*, 1984, **88**, 5903-5913.
65. H. Gerischer, *Electrochimica Acta*, 1990, **35**, 1677-1699.
66. R. A. Marcus, *Ann. Rev. Phys. Chem.*, 1964, **15**, 155-196.
67. R. Memming, in *Electron Transfer I*, 1994, vol. 169, pp. 105-181.
68. T. W. Hamann, F. Gstrein, B. S. Brunschwig and N. S. Lewis, *J. Am. Chem. Soc.*, 2005, **127**, 7815-7824.
69. A. T. Garcia-Esparza and K. Takanabe, *J. Mater. Chem. A*, 2016, **4**, 2894-2908.
70. J. Wang, J. Zhao and F. E. Osterloh, *Energ. & Envi. Sci.*, 2015, **8**, 2970-2976.
71. M. Rodríguez-Pérez, E. Canto, R. García-Rodríguez, A. T. De Denko, G. Oskam and F. Osterloh, *J. Phys. Chem. C*, 2018, **122**, 2582-2588.

72. O. C. Compton, C. H. Mullet, S. Chiang and F. E. Osterloh, *J. Phys. Chem. C*, 2008, **112**, 6202 -6208.
73. X. C. Wang, K. Maeda, X. F. Chen, K. Takanabe, K. Domen, Y. D. Hou, X. Z. Fu and M. Antonietti, *J. Am. Chem. Soc.*, 2009, **131**, 1680-1681.

TOC